Nano Energy xxx (xxxx) xxx

Contents lists available at ScienceDirect

Nano Energy

journal homepage: http://www.elsevier.com/locate/nanoen

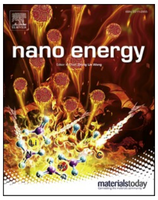

Full paper

High performance perovskites solar cells by hybrid perovskites co-crystallized with poly(ethylene oxide)

Kai Wang [1], Luyao Zheng [1], Tao Zhu, Lei Liu, Matthew L. Becker [**], Xiong Gong [*]

College of Polymer Science and Polymer Engineering, University of Akron, Akron, OH, 44325, United States

A R T I C L E I N F O

Keywords:
Hybrid perovskite
poly(ethylene oxide)
Hydrogen bonding
Photocurrent hysteresis
Power conversion efficiency
Stability

A B S T R A C T

Hybrid perovskite materials have emerged as attractive alternatives for cost-effective solar cells in the past ten years. However, achieving hysteresis-free, stable and efficient solution-processed perovskites solar cells has remained as a significant fundamental challenge. In this study, we report a strategy that utilizes poly (ethylene oxide) to sequester the counter ions in the perovskite lattices to suppress the formation of point defects, reduce the migration of ions/vacancy and to facilitate crystal growth in a more thermodynamically preferred orientation. Systematical investigations indicate that poly (ethylene oxide) indeed form hydrogen bonds with perovskite, which reduces the formation of kinetically-driven point defects, minimize charge carrier recombination and sharpen the density of states distribution. As a result, un-encapsulated solution-processed perovskite solar cells exhibit stabilized power conversion efficiency with hysteresis-free characteristics and significantly improved ambient shelf- and thermal-stability at relative high humidity, in comparison to the reference devices that exhibit unstable power conversion efficiency with dramatically higher hysteresis factor and poorer device lifetime. Our studies demonstrate that development of hybrid perovskite materials co-crystallized with polymers is an efficient approach towards high performance perovskite solar cells.

1. Introduction

Hybrid perovskite materials, with a typical formula of ABX_3, where $A = CH_3NH_3^+$ or $NH_2CH{=}NH_2^+$, $B = Pb^{2+}$ or Sn^{2+}, and $X = Cl^-$ or Br^- or I^- or their combination, have emerged as attractive alternatives for realizing cost-effective efficient perovskite solar cells (PSCs) in the past ten years [1,2]. Even though single crystal and large grain-size polycrystalline methylammonium lead halide (for example, $CH_3NH_3PbI_3$) thin films for efficient PSCs have been reported, intrinsically inevitable electronic and structural disorders, the ionic point-defects, the extended dislocations and grain boundaries still restrict the device performance of PSCs, with regard to efficiency, stability and hysteresis [1–9].

In the $CH_3NH_3PbI_3$ thin films, Schottky and Frenkel defects and the point vacancies of Pb^{2+}, I^- and $CH_3NH_3^+$ result in shallow donor and/or acceptor levels, and severe charge carrier recombination, lowering the short-circuit current density (J_{SC}) [7–9]. Moreover, the tail states near the conduction band broaden the density of state distribution, which results in low level quasi Fermi energy, reducing the open-circuit voltage (V_{OC}). Both theoretical and experimental studies demonstrated that the activation energies for ion migration in $CH_3NH_3PbI_3$ thin film are low (0.58 eV for I^- and 0.84 eV for $CH_3NH_3^+$) [10–12]. Such mobile ions and their corresponding I^- and $CH_3NH_3^+$ vacancies result in irreproducibility issues in the current density-voltage traces, termed as photocurrent hysteresis [13], in PSCs. In addition, the site-vacancies provide additional channels for moisture to diffuse into the crystal lattices, resulting in thermodynamically unstable hybrid perovskite materials [14]. Furthermore, the point defects and the ion migration/drift induce local perturbation of non-stoichiometric compounds and create local crystal lattice collapse [15], resulting in more unstable materials.

PSCs incorporated with various polymers for boosting device efficiencies have been reported (Supporting **Information 1 (SI 1))** [16–22]. Masi et al. utilized the low-molecular-weight organic gelators to facilitate the crystallization process for achieving higher quality perovskite active layer and obtained improved power conversion efficiency (PCE) (14.5%) and enhanced stability of PSCs [16]. Zhang et al. employed the electron donor polymer as the interfacial layer to passivate the trap of perovskite materials [17]. Zhao et al. and Sardashti et al. employed insulating polymers as the scaffold layers infiltrated with perovskite for

---

[*] Corresponding author.
[**] Corresponding author.
E-mail addresses: becker@uakron.edu (M.L. Becker), xgong@uakron.edu (X. Gong).
[1] These authors are contributed to this work equally.

https://doi.org/10.1016/j.nanoen.2019.104229
Received 29 August 2019; Accepted 23 October 2019
Available online 28 October 2019

efficient charge transport [18,19]. Bi et al. used poly (methyl methacrylate) as a template to foster an optimized crystallization of perovskite thin film and obtained an enhanced PCE from PSCs [21]. However, an in-depth understanding of the link between polymer with hybrid perovskite was rarely addressed.

To approach hysteresis-free, stable and efficient solution-processed PSCs, we report a strategy that utilizes poly (ethylene oxide) (PEO) to anchor $CH_3NH_3^+$ at the A-site and I^- at the X-site through the formation of the hydrogen interactions between PEO and $CH_3NH_3PbI_3$, suppressing the formation of the point defect and the migration of ions/vacancy. It is found that PEO can also facilitates the crystallization in a more thermodynamically preferred orientation, and consequently, sharpens the density of states distribution. As a result, un-encapsulated PSCs by solution-processed $CH_3NH_3PbI_3$ co-crystalized with PEO thin film exhibit stabilized PCE with hysteresis-free characteristics and significantly boost stability after being operated in air with 50% relative humidity in comparison to the reference devices that exhibit unstable power conversion efficiency with dramatically higher hysteresis factor and poorer device lifetime.

2. Material and methods

2.1. Materials

PEO with different molecular weight (M_w) ($M_w = 500$, 1000, and 4500 Da) was purchased from Scientific Polymer Inc [6,6].-Phenyl--C61-butyric acid methyl ester ($PC_{61}BM$) (99.5%) was purchased from Solenne BV. Lead iodide (PbI_2, 99.999%, beads), anhydrous N, N-dimethylformamide (DMF), dimethyl sulfoxide (DMSO), ethanol (99.5%), and chlorobenzene (99.8%) were purchased from Sigma-Aldrich. All chemicals were used as received without further purification.

2.2. Preparation of perovskite thin films

Both pristine $CH_3NH_3PbI_3$ and the PEO-$CH_3NH_3PbI_3$ thin films are prepared by the two-step method [23]. PbI_2 precursor solution was prepared by adding PbI_2 (400 mg, 0.87 mmol/mL) into a solution of DMF and DMSO (1 mL 97.5:2.5 v/v%). The PbI_2 precursor solution was mixed with the respective PEO solution adding PEO (10.0 mg) with different M_w. The M_w of the PEO materials are 500 Da, 1000 Da, and 4500 Da. Since PEO with $M_w > 4500$ Da are difficult to dissolve in DMF, PEO with $M_w > 4500$ Da was excluded in this study. For studies measuring the influence of PEO concentration, PEO with $M_w = 4500$ Da is selected, and the PEO concentrations were tuned from 1%, to 3%, 5%, and 10% (w% to PbI_2), respectively, while maintaining the PbI_2 concentration at 400 mg/mL (0.87 mmol/mL). Afterward, either PbI_2 layer or PbI_2 mixed with PEO precursor layer was firstly deposited on the substrates by spin-casted (3500 RPM, at 75 °C) method. And then MAI layer was deposited on the top of either PbI_2 layer or PbI_2 mixed with PEO precursor layer by spin-casting (3500 RPM) from MAI precursors solutions (35 mg/mL, 0.22 mmol/mL in ethanol), followed with thermal annealing at 100 °C for 2 h to create the final perovskite thin films. The details in preparation of PEO-$CH_3NH_3PbI_3$ thin films are described in **SI 2**.

2.3. Characterization of perovskite thin films

Fourier transform infrared (FTIR) spectra were acquired on an FTIR spectrometer (Alpha-P, Bruker Optics, Billerica, MA, U.S.A.) in transmission mode. The samples for FTIR measurements were prepared through scratching thin films of PEO, $CH_3NH_3PbI_3$ and PEO-$CH_3NH_3PbI_3$ from ITO (indium tin oxide) substrates, and the obtained powders were mixed with KBr to form disc under high pressure. The X-ray diffraction (XRD) patterns of pristine $CH_3NH_3PbI_3$ and the PEO-$CH_3NH_3PbI_3$ powders were measured by using a Bruker AXS Dimension D8 X-ray system. The grazing-incidence wide-angle x-ray scattering (GIWAXS) was performed on the high-resolution GIWAXS beamline (Sector 8-ID-E) in the Advanced Photon Source, Argonne National Laboratory [24]. X-ray photon energy was fixed at 7.35 keV. Two incidence angles of 0.2° or 0.4° (either smaller or larger than the critical angle of total external reflection for silicon or perovskite, meanwhile at the 0.4°, the penetration depth is still in the range of the perovskite film thickness thus the substrate influence can also be neglected) were used to check the scattering from film surface or the bulk film, respectively. As-cased perovskite films on silicon wafer were mounted on a heating stage, which was connected with a temperature controlling system. The samples and the heating stage were an Argon atmosphere to eliminate the moisture or oxygen influence on perovskite during the measurement. Pilatus 1 M (Dectris Ltd.), a single-photon-counter area detector, mounted at the position either 212.4 mm downstream from the sample, was used to collect GIWAXS patterns. The GIWAXS data were collected by exposing the samples in X-ray for 3 s, and analyzed by using a Matlab based software (GIXSGUI). The thermal annealing process was as follows: a) the annealing temperature was kept at 20 °C for 30 min (min) then raised to 40 °C in 10 min, b) the annealing temperature was kept at 40 °C for 30 min then raised to 80 °C in 10 min, c) the annealing temperature was kept at 100 °C for 30 min then raised to 120 °C in 10 min, d) the annealing temperature was kept at 120 °C for 30 min. During each stable temperature-stage of 20 °C, 40 °C, 80 °C, and 120 °C, the GIWAXS data were collected. The as-cased sample of PEO-$CH_3NH_3PbI_3$ was prepared as described, where the M_w of PEO is 4500 Da, and the concentration is 5% in precursor solution. UV–vis absorption spectra of thin films were measured using the HP 8453 spectrophotometer in air. The top view scanning electron microscopy (SEM) images were obtained by using a field-emission scanning electron microscope (JEOL-7401).

2.4. Fabrication of PSCs

The ITO glass was cleaned by detergent, deionized water, acetone and isopropanol sequentially. Then, the ITO-glasses were dried in an oven at 100 °C overnight. The pre-cleaned ITO substrates were then treated with UV-ozone for 40 min (mins) under an ambient atmosphere. Then, a ~40 nm thick film of NiO_x was spin-casted on the top of ITO substrates from NiOx precursor solution. Either pristine $CH_3NH_3PbI_3$ thin film or the PEO-$CH_3NH_3PbI_3$ thin film was deposited on the top of NiO_x layer via two-step method described above. Afterward, a 40 nm-thick $PC_{61}BM$ layer was spin-cased on top of perovskite layer from a 20 mg/mL chlorobenzene solution. Last, a 120 nm-thick aluminum (Al) film was deposited through a shadow mask in the vacuum with base line of $\sim 2 \times 10^{-6}$ mbar atmosphere. The device area was measured to be 0.16 cm^2.

2.5. Characterization of PSCs

The photocurrent density verses voltage (J-V) characteristics of PSCs were obtained by using a Keithley model 2400 source measure unit. A Newport Air Mass 1.5 Global (AM1.5G) full-spectrum solar simulator was applied as the light source. The light intensity was 100 mW/cm^2, which was calibrated using a monosilicon detector (with a KG-5 visible color filter) from the National Renewable Energy Laboratory to reduce the spectral mismatch. The incident photon-to-current efficiency (IPCE) spectra of PSCs was measured through a solar cell quantum efficiency measurement system in use at European Solar Test Installation (ESTI) for cells and mini-modules: a 300 W steady-state xenon lamp provides the source light; up to 64 filters (8–20 nm width, range from 300 to 1200 nm) are available on four filter-wheels to produce the monochromatic input, which is chopped at 75 Hz, superimposed on the bias light and measured via the usual lock-in technique; bias light is necessary to put the device under examination close to the operating irradiance condition. After collecting the IPCE data, the software also integrates the data with the AM1.5G spectrum and gives the calculated

J_{SC} value. The transient photocurrent (TPC) measurements were conducted in a custom built, fully-automated setup [25]. Impedance spectra were recorded by a HP 4194A impedance/gain-phase analyzer with an oscillating voltage of 10 mV from 0.5 Hz to 1 MHz.

3. Results and discussion

The oxygen atom in the backbone of PEO with $CH_3NH_3^+$ at the crystal-A-site can form the hydrogen bond '$O\cdots H–NH_2CH_3^+$', and the hydroxyl at the end of PEO with I^- at the crystal-X-site in the PbI_6 octahedra framework can form the hydrogen bond '-OH…I-' (**SI 3**) [26, 27]. Fig. 1a presents the FTIR spectra of PEO, $CH_3NH_3PbI_3$ and PEO-$CH_3NH_3PbI_3$ thin films. Similar to PEO, the PEO-$CH_3NH_3PbI_3$ thin film exhibits a wide 'O–H' stretching vibration, which is attributed to the inter- and intra-molecular hydrogen bonds. Moreover, $CH_3NH_3^+$ shows a 'N–H' stretching band with a half width at half maximum (HWHM) of 301 cm^{-1} in the PEO-$CH_3NH_3PbI_3$ thin film compared to that of 185 cm^{-1} in pristine $CH_3NH_3PbI_3$ thin film. Collectively, these results demonstrate that the backbone of PEO with $CH_3NH_3^+$ at the crystal-A-site indeed form a hydrogen interaction of '$O\cdots H–NH_2CH_3^+$'. However, the hydrogen bonding interaction of '-OH…I-' is too weak to be detected by FTIR spectroscopy [28]. Towards the end, a proton nuclear magnetic resonance (^1H NMR) spectroscopy titration measurement was carried out to confirm the interactions of '-OH…I-' and '$O\cdots H–NH_2CH_3^+$'. Fig. 1b compares ^1H NMR spectra of the deuterated PEO, $CH_3NH_3PbI_3$ and PEO-$CH_3NH_3PbI_3$ dimethyl sulfoxide solutions (**SI 4**). For PEO solution, two methylene groups between the oxygen atom in the main-chain ($–(OCH_2CH_2)_n–$) are characterized by the peak at $\delta = 3.51$ p.p.m. (denoted by "*a*" in Fig. 1b) and the hydroxyl group (-OH) at the end of polymer chain is characterized by the peak at $\delta = 4.59$ p.p.m. (denoted by "*b*" in Fig. 1b). The resonance response corresponding to the $CH_3NH_3^+$ group in the $CH_3NH_3PbI_3$ solution is located around $\delta = 7.42$ p.p.m. (denoted by "*c*" in Fig. 1b). Due to the multiple spatial conformation of the $CH_3NH_3^+$ cation inside the crystallographic lattice, spilt peaks of the $CH_3NH_3^+$ signal are found in the magnified NMR spectra (**SI 4).** For the PEO-$CH_3NH_3PbI_3$ solution, the protons from the methylene groups in the PEO main-chain show a small up-field shift of $\Delta\delta \approx$-0.2 p.p.m., corresponding to the "*a**" in Fig. 1b. Because the influence of the oxygen atom on the protons of methylene is weak [28], the formation of hydrogen bonds between $CH_3NH_3^+$ and the oxygen atom in PEO chain hence leads to such a small chemical shift. However, the protons from the end group of PEO chain show a large up-field shift of $\Delta\delta \approx$-1.4 p.p.m. (denoted by "*b**" in Fig. 1b (also in **SI 4**), which is ascribed to the direct hydrogen interaction of '-OH…I-' [29]. Similarly, the resonance signals arising from the $–NH_3^+$ protons of PEO-$CH_3NH_3PbI_3$ also undergo a significant up-field shift of $\Delta\delta \approx$-0.3 p.p.m. (denoted by "*c**" in Fig. 1b), which further verifies the '$O\cdots H–NH_2CH_3^+$' hydrogen-bonding interaction. Moreover, the broadened *c** in the PEO-$CH_3NH_3PbI_3$ is also a positive indication of the hydrogen bond formation. The formation of '$O\cdots H–NH_2CH_3^+$' would increase the conformational complexity of hydrogen atom in the crystal lattice, which is consistent with the resonance peak broadening of *c**. Thus, these results demonstrate the confirmation of the intramolecular interaction of '$O\cdots H–NH_2CH_3^+$' and '-OH…I-' between PEO and $CH_3NH_3PbI_3$. Such intramolecular

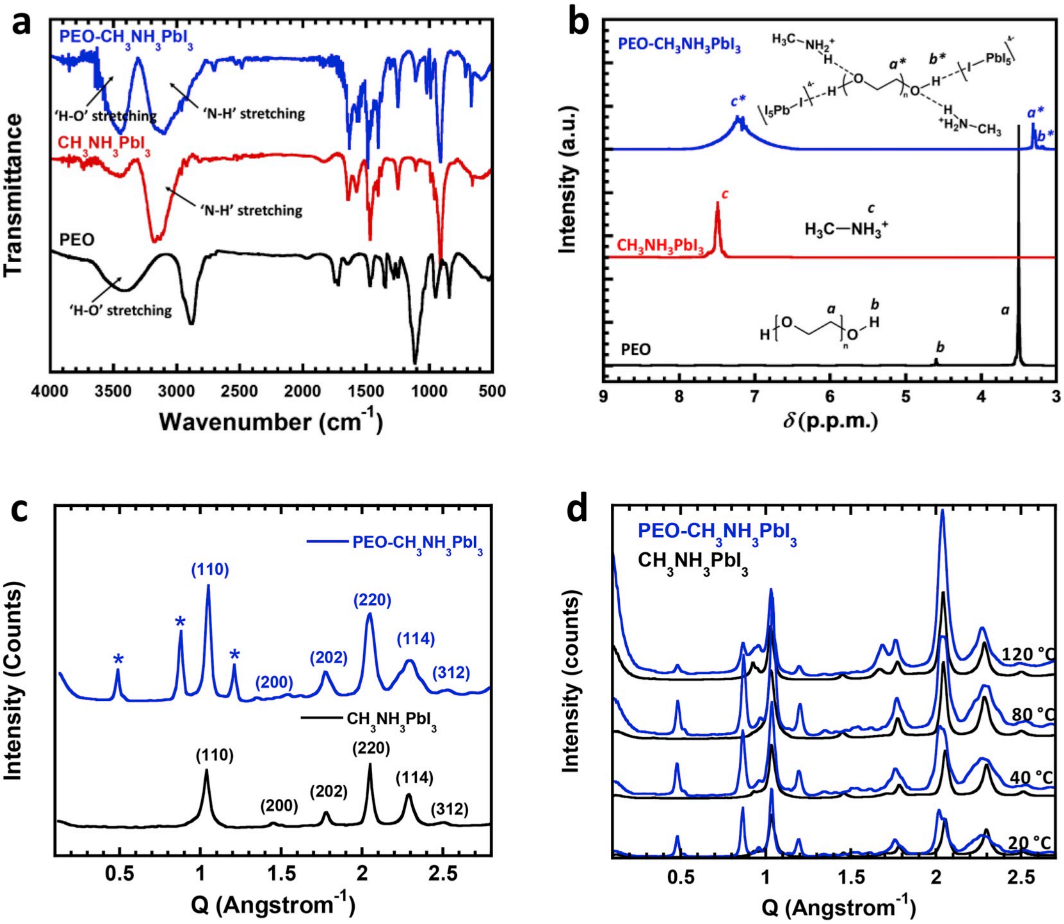

Fig. 1. (a) The FTIR spectra of PEO, $CH_3NH_3PbI_3$ and PEO-$CH_3NH_3PbI_3$thin films, (b) the NMR spectra for PEO, $CH_3NH_3PbI_3$ and PEO-$CH_3NH_3PbI_3$ solutions, (c) the XRD patterns of PEO-$CH_3NH_3PbI_3$ and $CH_3NH_3PbI_3$ powders (asterisked peaks are induced by intermolecular interactions between the PEO and the perovskite, which raise the structural complexity in the PEO-$CH_3NH_3PbI_3$) and (d) the azimuthally integrated in-situ GIWAXS patterns of pristine $CH_3NH_3PbI_3$ thin film and the PEO-$CH_3NH_3PbI_3$ thin film annealed at different temperatures.

interaction suggested that the activation energies for I^- and $CH_3NH_3^+$ migration in the PEO-$CH_3NH_3PbI_3$ thin film are higher than those in pristine $CH_3NH_3PbI_3$ thin film [14].

Fig. 1c displays XRD patterns of pristine $CH_3NH_3PbI_3$ and the PEO-$CH_3NH_3PbI_3$ powders. Similar to pristine $CH_3NH_3PbI_3$, the PEO-$CH_3NH_3PbI_3$ powder exhibits the characteristic scattering peaks located at the (110), (200), (202), (220), (114), (312) planes indicate that perovskite is with a tetragonal structure, which is in good agreement with other reports [30,31]. It is noteworthy that the crystallization of pristine PEO is featured by a *d*-spacing of ~4 Å, corresponding to a scatter vector (*q*) ranging from ~1.4 to ~1.8 $Å^{-1}$ [32,33]. As shown in Fig. 1c, no obvious scattering peaks of PEO crystals were found in the PEO-$CH_3NH_3PbI_3$ powder, suggesting a well-dispersion of PEO inside of the perovskite lattice without isolated PEO aggregations. Interestingly, there are three additional peaks (asterisked in Fig. 1c) at the scattering vector q = 0.49, 0.88 and 1.21 $Å^{-1}$ in the PEO-$CH_3NH_3PbI_3$ powder. Moreover, the PEO-$CH_3NH_3PbI_3$ powder also exhibits broader perovskite peaks located at the (202), (220), and (114) planes, which are ascribed to the strong intermolecular interactions between PEO and perovskite lattice [34,35]. As the formation of hydrogen bonds could stretch and regulate the crystal lattice in certain degrees, changing the *d*-spacing and even inducing new scattering planes [34,35]. Consequently, the observations of multiple peaks in the XRD spectrum of the PEO-$CH_3NH_3PbI_3$ powder are consistent with the elevated chemical complexity induced by the polymer additive, which further confirm the formation of the intermolecular hydrogen interactions among them.

Fig. 1d presents the quantified azimuthally integrated intensities for both pristine $CH_3NH_3PbI_3$ and the PEO-$CH_3NH_3PbI_3$ thin films annealed at different temperatures, based on the in-situ GIWAXS profiles (**SI 5**). As the annealing temperatures are increased, the scattering intensities of the perovskite scattering features for both thin films are increased. Even at a high temperature of 120 °C, the scattering rings induced by the '-OH…I-' interaction are still remained (**SI 5**), indicating that the PEO-$CH_3NH_3PbI_3$ thin film possesses a relatively high thermal stability compared to pristine $CH_3NH_3PbI_3$ thin film.

Fig. 2a–d presents the top-view SEM images of pristine $CH_3NH_3PbI_3$ thin film and the PEO-$CH_3NH_3PbI_3$ thin film, where PEO are with different weight-average-molecular-masses (M_w). Pristine $CH_3NH_3PbI_3$ thin film possesses a large number of defects and voids; whereas the PEO-$CH_3NH_3PbI_3$ thin films exhibit dramatically reduced numbers of pin-holes and grain boundaries, as well as a wide-range evolution of thin film morphologies and topographies, which are from "dot"-like (PEO ~ M_w = 500 Da), to "fiber"-like (PEO ~ M_w = 1000 Da), and even to "bulk"-like polycrystals (PEO ~ M_w = 4500 Da). The effect of M_w on the film morphology is probably attributed to the retarded crystal growth processes induced by hydrogen interactions in the PEO-$CH_3NH_3PbI_3$ thin film [36,37]. As M_w increases, the '$O\cdots H–NH_2CH_3^+$' hydrogen bonding interactions would be enhanced, forming intermediate adducts, which would reduce the crystal growth rate and eventually result in larger crystal domains [38]. Such film morphological change is further verified by the scattering characterizations (**SI 5**). Noted that PEO with M_w > 4500 Da is excluded in this study since such high M_W PEO is poorly soluble in the CH_3NH_3I precursor solution and undissolved PEO results in inferior perovskite film morphology (**SI 6**). Thus, PEO with M_w = 4500 Da is used for making the PEO-$CH_3NH_3PbI_3$ thin films to further investigating its film morphologies and photovoltaic properties.

Fig. 2e–h displays the top-view SEM images of the PEO-$CH_3NH_3PbI_3$ thin films, where the concentrations of PEO (M_w = 4500 Da) are varied from 1%, 3%, 5% and 10%. It is found that the crystalline grain sizes are increased from ~300 nm to ~700 nm, ~1500 nm and ~1250 nm for the PEO-$CH_3NH_3PbI_3$ thin films, where the corresponding PEO concentrations are from 1%, 3%, 5% and 10%, respectively. It is noteworthy to mention that the burned residual PEO by the high energy electron beam result in the hollow feature in the PEO-$CH_3NH_3PbI_3$ thin film with high concentration (larger than 10%) (**SI 6**). To further confirm it, lower voltage and faster scan-mode are applied for conducting SEM. It is found that only at high concentration (e.g., 10% of PEO), PEO starts to aggregate on top of the perovskite polycrystals, which could result in increased series resistance, hampering the charge transport in PSCs. Thus, larger grain size and reduced grain boundary indicate that the PEO-$CH_3NH_3PbI_3$ thin film incorporated with 5% of PEO (M_w = 4500 Da) possess optimal electronic properties.

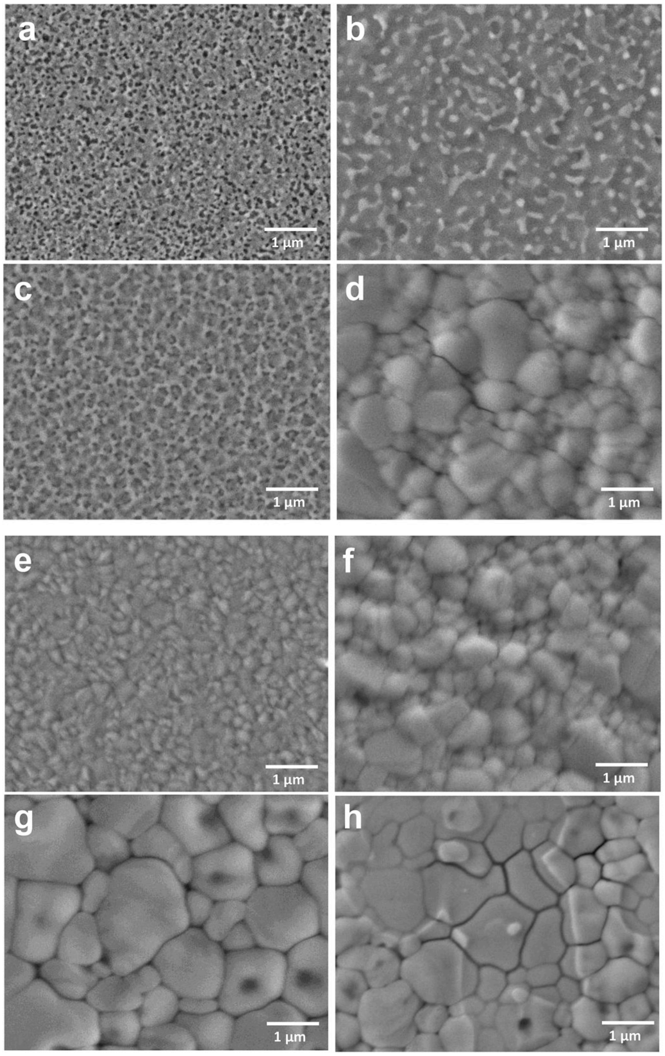

Fig. 2. The top-view SEM images of (a) pristine $CH_3NH_3PbI_3$ thin film and the PEO-$CH_3NH_3PbI_3$ thin films, where PEO with M_w of (b) 500 Da, (c) 1000 Da and (d) 4500 Da, and the top-view SEM images of the PEO-$CH_3NH_3PbI_3$ thin films, where PEO with M_w of 4500 Da, but with concentrations of (e) 1%, (f) 3%, (g) 5% and (h) 10%.

The photovoltaic properties of the PEO-$CH_3NH_3PbI_3$ thin film are investigated through the evaluation of device performance of PSCs with a planar heterojunction device structure of ITO/NiO_x/$CH_3NH_3PbI_3$ (or PEO-$CH_3NH_3PbI_3$)/$PC_{61}BM$/Al, where ITO acts as the anode electrode, solution-processed NiO_x thin film is used as the hole extraction layer (HEL), $PC_{61}BM$ acts as the electron extraction layer, Al acts as the cathode electrode, respectively. Fig. 3a and b shows the J-V characteristics of PSCs by either pristine $CH_3NH_3PbI_3$ thin film or the PEO-$CH_3NH_3PbI_3$ thin film. Under one-sun illumination with the light intensity of 100 mW/cm^2, at the scan rate of 0.10 V/s and the reverse scan direction, the PSCs by pristine $CH_3NH_3PbI_3$ thin film exhibit a J_{SC} of 21.08 mA/cm^2, a V_{OC} of 1.05 V and a fill factor (FF) of 74.7%, with a corresponding PCE of 16.53%. Whereas, the PSCs by the PEO-$CH_3NH_3PbI_3$ thin film, where M_w of PEO is 4500 Da and the

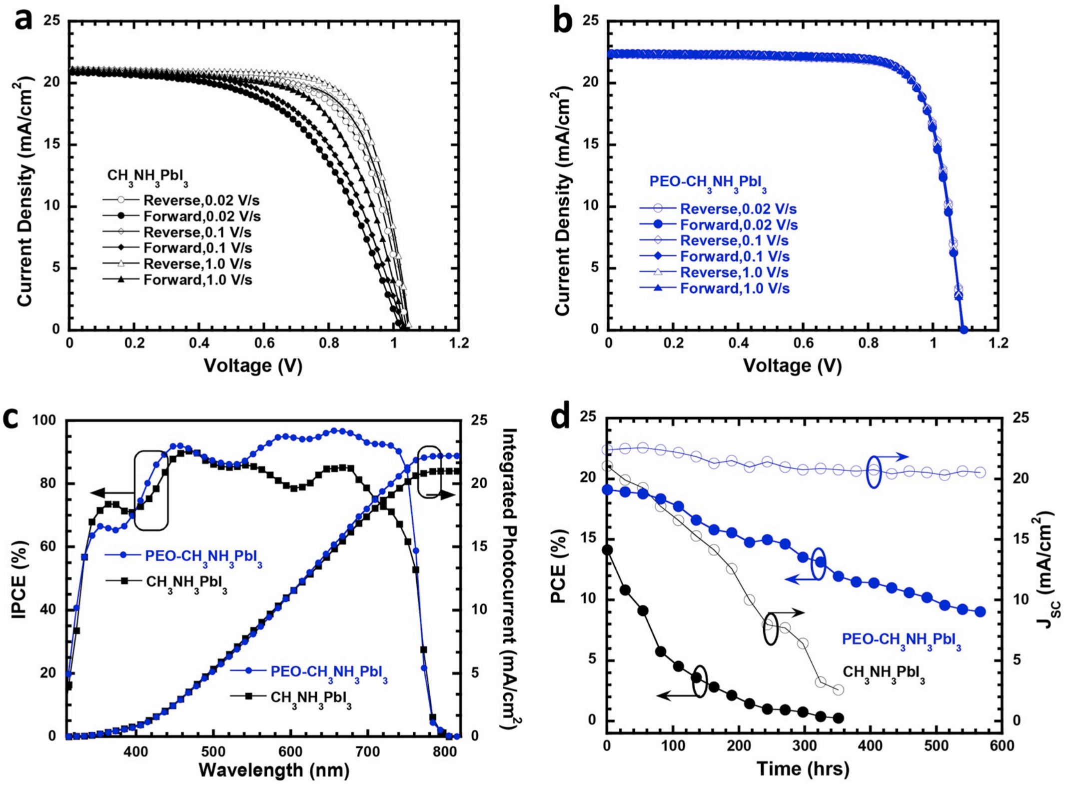

Fig. 3. The J-V characteristics of the PSCs by (a) pristine $CH_3NH_3PbI_3$ thin film, and (b) the PEO-$CH_3NH_3PbI_3$ thin film under different scan directions and the different scan rates, (c) the IPCE spectra and integrated J_{SC} of the PSCs by either pristine $CH_3NH_3PbI_3$ thin film or the PEO-$CH_3NH_3PbI_3$ thin film, and (d) PCE and J_{SC} values of unencapsulated PSCs by either pristine $CH_3NH_3PbI_3$ thin film or the PEO-$CH_3NH_3PbI_3$ thin film, measured at room temperature in an ambient condition with 50% relative humidity.

concentration of PEO is 5%, exhibit a J_{SC} of 22.38 mA/cm^2, a V_{OC} of 1.10 V and a FF of 77.8%, with a corresponding a PCE of 19.15%, which is the highest PCE among all PSCs (**SI 7**).

It is interesting that under different scan conditions, *i.e.,* scan rate ranges from 0.02 V/s to 1.00 V/s with both reverse and forward scan directions, dramatic differences in J-V characteristics are observed (Fig. 3a and b). The PSCs by the PEO-$CH_3NH_3PbI_3$ thin film possess consistent J-V characteristics in regardless of scan rates and scan directions, whereas the PSCs by pristine $CH_3NH_3PbI_3$ thin film possess severe scan-condition-dependent J-V characteristics. The scan condition effects on the photocurrent behaviors in PSCs typically terms as the photocurrent hysteresis [13,39,40], which is quantified by a dimensional hysteresis index (*HI*) [39],

$$HI = (J_{scan-} V_{OC} / 2 - J_{scan+} V_{OC} / 2)/(J_{scan-} V_{OC} / 2) \quad (1)$$

(where J_{scan-} $V_{OC}/2$ is the photocurrent density at $V_{OC}/$ 2 bias for the reverse scan, while J_{scan+} $V_{OC}/2$ is the photocurrent density at $V_{OC}/$ 2bias for the forward scan). High *HI* values ranging from 0.025 to 0.045 are observed from the PSCs by pristine $CH_3NH_3PbI_3$ thin film; whereas, *HI* of 0.001, a negligible value, is observed from the PSCs by the PEO-$CH_3NH_3PbI_3$ thin film. To further investigate the photocurrent hysteresis, the steady-state efficiency under the stabilized photocurrent at the maximum power voltage is conducted. The ratios of the steady-state efficiency versus the scan efficiency are 0.995 and 0.910 for the PSCs by either the PEO-$CH_3NH_3PbI_3$ thin film or pristine $CH_3NH_3PbI_3$ thin film, respectively (**SI 8**). The studies of the frequency-dependent capacitance of PSCs in dark (**SI 8**) demonstrate that both PSCs show a capacitance of $\sim 10^{-6}$ F cm^{-2} at low frequency, indicating that capacitance is correlated to the chemically reactive sites at the interface [41]. It is also found that the PSCs fabricated by the PEO-$CH_3NH_3PbI_3$ thin film exhibit a lower capacitance than that by pristine $CH_3NH_3PbI_3$ thin film, implying that the PEO-$CH_3NH_3PbI_3$ thin film possessing lower reactive sites. The reduced reactive sites are probably attributed to the interactions between PEO and ions in perovskite, implying that the ions were less mobile in PSCs fabricated by the PEO-$CH_3NH_3PbI_3$ thin film. Thus, the PSCs by the PEO-$CH_3NH_3PbI_3$ thin film exhibit hysteresis-free characteristics.

Fig. 3c presents the IPCE spectra of PSCs with corresponding integrated J_{SC}. The integrated J_{SC} of the PSCs by pristine $CH_3NH_3PbI_3$ thin film and the PEO-$CH_3NH_3PbI_3$ thin film are 20.91 mA/cm^2 and 22.03 mA/cm^2, respectively. These values are consistent with J_{SC} (21.08 mA/cm^2 for the PSCs by pristine $CH_3NH_3PbI_3$ thin film, 22.38 mA/cm^2 for the PSCs by the PEO-$CH_3NH_3PbI_3$ thin film extracted from the J-V characteristics (Fig. 3a and b). It is found that the PSCs by the PEO-$CH_3NH_3PbI_3$ thin film exhibit a significantly enhanced IPCE in the wavelength from 550 nm to 750 nm. The enhanced absorption intensity, increased charge generation, and improved charge transport could account for the efficient charge dissociation in the PSCs by the PEO-$CH_3NH_3PbI_3$ thin film. The detailed discussion is described in their correspondingly absorption spectrum, transient photocurrent, and impedance spectrum.

Fig. 3d presents the shelf-stability of PSCs, where un-encapsulated PSCs are tested at room temperature in an ambient condition with 50% relative humidity (also **SI 9**). The PSCs by pristine $CH_3NH_3PbI_3$ thin film exhibit a rapid decrease in J_{SC}, PCE and V_{OC}, FF during the aging process, with a half shelf-lifetime of 69 h); whereas the PSCs by the PEO-$CH_3NH_3PbI_3$ thin film exhibit a dramatically alleviate decay rate and a significantly extended half shelf-lifetime of 504 h. The thermal stabilities of un-encapsulated PSCs are also tested by aging the devices at elevated temperatures of 300 K, 335 K, 355 K and 375 K in ambient condition with 60–70% relative humidity (**SI 10**). It is found that the PSCs by the PEO-$CH_3NH_3PbI_3$ thin film are more thermally stable than that by pristine $CH_3NH_3PbI_3$ thin film. Such thermally stable PSCs is attributed to the formation of hydrogen bonds between PEO and perovskite lattice. As temperature increases, the kinetic vibration (thermal energy) is first absorbed by the hydrogen bond as its bonding energy is typically lower than that of covalent or ionic bonds within the perovskite lattice. In this manner, the hydrogen interaction protects whole perovskite layer in certain degrees against the heat, rendering higher thermal stability.

Notice that we also investigate PSCs with a device structure of ITO/PTAA/$CH_3NH_3PbI_3$ (or PEO-$CH_3NH_3PbI_3$)/$PC_{61}BM$/Al, where PTAA is poly[bis(4-phenyl) (2,4,6-trimethylphenyl)amine] and acts the HEL instead of solution-processed NiOx HEL (**SI 7**). PSCs by pristine $CH_3NH_3PbI_3$ thin film exhibit a J_{SC} of 22.18 mA/cm^2, a V_{OC} of 1.04 V, a FF of 0.71, with a corresponding PCE of 16.49%, whereas PSCs by the PEO-$CH_3NH_3PbI_3$ thin film exhibit a J_{SC} of 23.01 mA/cm^2, a V_{OC} of 1.12 V, a FF of 0.81, with a corresponding PCE of 20.78%, which is more than 26% as compared with that from PSCs by pristine $CH_3NH_3PbI_3$ thin film. Moreover, PSCs by pristine $CH_3NH_3PbI_3$ thin film possess an HI of 1.98%, whereas PSCs by the PEO-$CH_3NH_3PbI_3$ thin film possess an HI of 0.001%. These results indicate that whereas PSCs by the PEO-$CH_3NH_3PbI_3$ thin film exhibit photocurrent hysteresis-free characteristics.

The TPC measurement is conducted to investigate the charge generation and transport kinetics in PSCs. Fig. 4a presents the normalized photocurrent decays of PSCs as a function of time, where PSCs is biased at −2 V for ensuring all separated charge carriers to be collected by the electrodes. Under the short-circuit condition, both PSCs possess a similar TPC curve. At the beginning, the curve tends to be linear because most charge carriers are extracted within a relatively short time and then followed by a long tail. Such long tails are originated from charge carriers that experience the trap and de-trap processes [25]. By extrapolating the linear region to zero, the charge extraction lifetime is estimated [42]. The PSCs by the PEO-$CH_3NH_3PbI_3$ thin film exhibit a shorter carrier extraction time of 75 ns (ns), which is shorter than 110 ns from the PSCs by pristine $CH_3NH_3PbI_3$ thin film, indicating less charge carrier recombination occurs in the PSCs fabricated by the PEO-$CH_3NH_3PbI_3$ thin film [43,44]. On the other hand, the PSCs fabricated by either pristine $CH_3NH_3PbI_3$ thin film or the PEO-$CH_3NH_3PbI_3$ thin film have a similar charge carrier sweep-out process. The charge carrier sweep-out is very fast at the beginning, but a significant difference occurs after a 50 ns interval. There is an almost 15% of more charge carriers are swept-out in the PSCs fabricated by the PEO-$CH_3NH_3PbI_3$ thin film compared to that by pristine $CH_3NH_3PbI_3$ thin film (**SI 7**), indicating that the PSCs fabricated by the PEO-$CH_3NH_3PbI_3$ thin film exhibits a higher PCE than that by pristine $CH_3NH_3PbI_3$ thin film [44].

To further understand the improvement of device performance, the point defects within the crystal lattice by counter ions, and the structural in-continuity with less boundaries and pin-hole impurities by large crystal domains in both pristine $CH_3NH_3PbI_3$ and the PEO-$CH_3NH_3PbI_3$

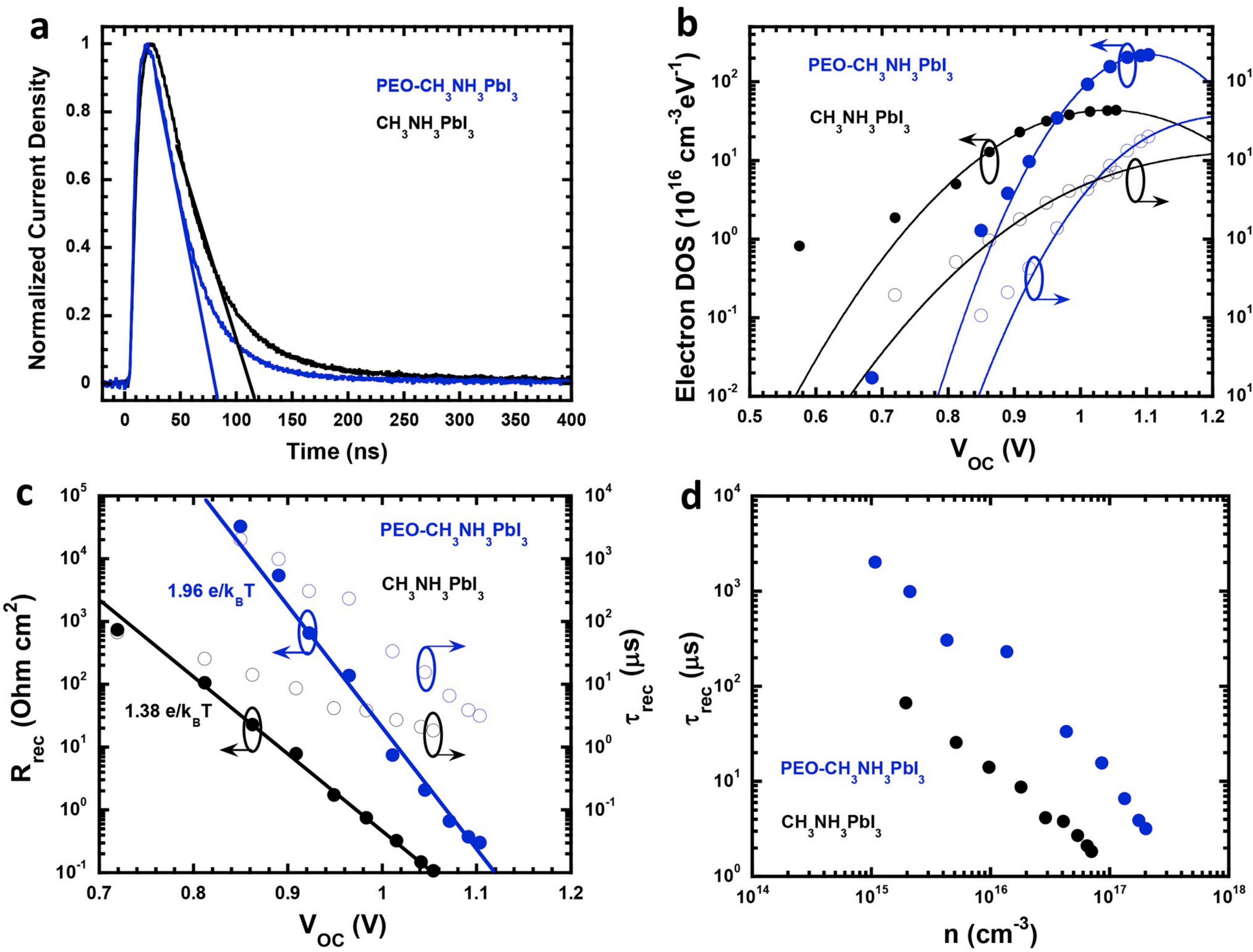

Fig. 4. (a) The TPC curves of the PSCs by either pristine $CH_3NH_3PbI_3$ thin film or the PEO-$CH_3NH_3PbI_3$ thin film, (b) the electron DOS distribution and the charge carrier density generated in the PSCs by pristine $CH_3NH_3PbI_3$ thin film or the PEO-$CH_3NH_3PbI_3$ thin film at different V_{OC} conditions, (c) the recombination resistance and lifetime verses V_{OC} and (d) the recombination lifetime verses the charge carrier density of the PSCs by pristine $CH_3NH_3PbI_3$ thin film or the PEO-$CH_3NH_3PbI_3$ thin film.

thin films are investigated by the density of state (DOS) distribution (**SI 11**). The DOS distribution, *g(n),* is determined by the chemical capacitance, (C_μ), which is described as [45]:

$$C_\mu = q^2 \int_{-\infty}^{E_{Fn}} dg \Big/ dEdE = q^2 g(E_{Fn}) \tag{2}$$

(where q is the elementary charge and E_{Fn} is the Fermi level). The C_μ is correlated with the homogeneous accumulation of charge carriers in photoactive layer. The C_μ is further described as [46]:

$$C_\mu^{(n)} = Lq^2 dn \big/ dE_{Fn} \tag{3}$$

(where n is the charge carrier density, L is the thickness of active layer). For a solar cell operated at V_{OC}, no charge is being collected at the electrodes. As a result, a change of C_μ is resulted from a variation of the Fermi energy due to a variation of the charge carrier density in photoactive layer.^{44} Thus, the differential of the electronic states of different photoactive layers can be used to verify the DOS distributions through the Gaussian approximation, (g_n). The g_n is expressed as [47,48]:

$$g_n(E - E_L) = N_n \Big/ \sqrt{2\pi}\sigma_n \exp\left[-\left(E - E_L\right)^2 \Big/ 2\sigma_n^2\right] \tag{4}$$

(where N_n is a total density per unit volume, E_L is the center of DOS, and σ_n is the disorder parameter). Fig. 4b presents the DOS distribution and the charge carrier densities generated in PSCs at different V_{OC}. A smaller σ_n of 121 meV is observed from the PSCs by the PEO-$CH_3NH_3PbI_3$ thin film as compared with 231 meV from the PSCs by pristine $CH_3NH_3PbI_3$ thin film, demonstrating that the PSCs by the PEO-$CH_3NH_3PbI_3$ thin film exhibit a narrower DOS distribution. Moreover, a N_n of 9×10^{19} cm^{-3} is observed from the PSCs by the PEO-$CH_3NH_3PbI_3$ thin film, which is higher than that (4×10^{19} cm^{-3}) from the PSCs by pristine $CH_3NH_3PbI_3$ thin film, indicating the total DOS of the PSCs by the PEO-$CH_3NH_3PbI_3$ thin film is enhanced. Thus, enlarged N_n and reduced σ_n are attributed to the effect of PEO on the PEO-$CH_3NH_3PbI_3$ thin film, which results in not only decreased point defects, but also templated large crystal domains with minimized boundaries and/or structural in-continuity. As a result, the PSCs by the PEO-$CH_3NH_3PbI_3$ thin film exhibit enhanced J_{SC} and enlarged FF, consequently, a boosted PCE.

Fig. 4c presents the recombination resistance (R_{rec}) for PSCs. The R_{rec} is related to the recombination current density, j_{rec}, which can be extracted from impedance measurement at low frequency part, and is described as [49]:

$$R_{rec} = 1/A\ (dj_{rec}/dV_{OC})^{-1} \tag{5}$$

(where A is active device area). The R_{rec} can thus be related to V_{OC} in terms of the recombination order parameter as:

$$R_{rec} = R_0\ \exp(-e\beta / k_B T\ V_{OC}(I)) \tag{6}$$

(where R_0 is a constant, e is the electron charge, β is the recombination order parameter, k_B is the Boltzmann constant, T is the absolute temperature, I is the light intensity). The PSCs by the PEO-$CH_3NH_3PbI_3$ thin film exhibit a β of 1.96, closing to 2, a theoretical value representing the second order charge carrier recombination mechanism dominated in solar cells [50,51]. In comparison, the PSCs by pristine $CH_3NH_3PbI_3$ thin film exhibit a β of 1.38, indicating the shallow trap-induced first order charge carrier recombination mechanism dominated in solar cells [52]. These are in good agreement with the results of improved charge transport properties (**SI 12**) of the PEO-$CH_3NH_3PbI_3$ thin film, which leads to less recombination loss on the way of charge transport. Therefore, the PSCs by the PEO-$CH_3NH_3PbI_3$ thin film possess better device performance than that by pristine $CH_3NH_3PbI_3$ thin film.

In addition, the recombination lifetime as a function of V_{OC} is further calculated by $\tau = R_{rec}C_\mu$ [53]. The recombination lifetime is the average time for the bimolecular electron-hole recombination in the photoactive layer. As shown in Fig. 4c, a longer carrier lifetime over a wide range of photovoltages is observed from the PSCs by the PEO-$CH_3NH_3PbI_3$ thin film compared to that by pristine $CH_3NH_3PbI_3$ thin film. Specifically, under one sun illumination, the recombination lifetime of the PSCs by the PEO-$CH_3NH_3PbI_3$ thin film is $\tau = 4.2$ μs, which is longer than $\tau = 1.5$ μs from the PSCs by pristine $CH_3NH_3PbI_3$ thin film. Such elongated charge carrier recombination lifetime is attributed to reduced defects and traps states in the PEO-$CH_3NH_3PbI_3$ thin film. Fig. 4d shows the recombination lifetime (τ) dependence on the charge carrier density n. As compared with that by pristine $CH_3NH_3PbI_3$ thin film, longer charge carrier lifetime observed from the PSCs by the PEO-$CH_3NH_3PbI_3$ thin film indicates that less charge recombination occurred in PSCs. Thus, the PSCs by the PEO-$CH_3NH_3PbI_3$ thin film possess high J_{SC}.

Charge carrier recombination with different scale in PSCs (Fig. 4c) are corresponding to different filling of the electronic states in the DOS, which result in various electron quasi Fermi levels [54]. Moreover, different DOS distributions in PSCs (Fig. 4b) indicate that different quasi Fermi levels (E_{Fn}) are present in pristine $CH_3NH_3PbI_3$ thin film and the PEO-$CH_3NH_3PbI_3$ thin film (**SI 11**) [55]. A wider DOS distribution in the PSCs by pristine $CH_3NH_3PbI_3$ thin film indicates that more electrons would accumulate at the lower-lying sub-bands, resulting in smaller V_{OC}. In addition, the loosely packed $CH_3NH_3PbI_3$ thin film yields less photo-generated electrons, which also sacrifice V_{OC} because the charge carrier density is positively correlated with V_{OC} (**SI 11**). Whereas, an elevated quasi Fermi level observed from the PSCs by the PEO-$CH_3NH_3PbI_3$ thin film would result in enlarged V_{OC} [56]. Thus, the PSCs by the PEO-$CH_3NH_3PbI_3$ thin film exhibit higher V_{OC} compared to that by pristine $CH_3NH_3PbI_3$ thin film.

The photocurrent hysteresis in PSCs was claimed to be a multifactorial phenomenon including multi-interfacial electronic behaviors, trapping/detrapping effects, ferroelectric effects, measuring conditions, as well as atmospheric conditions [12,13,38,40]. Fig. 5a presents the photocurrent rising processes of PSCs. Under white light illumination, slow rising (~20 s) of photocurrent to the maximum value indicates a synergistic process of balancing the trap-filling and ion/vacancy migration in the PSCs by pristine $CH_3NH_3PbI_3$ thin film; whereas, an instant photocurrent response upon white light illumination observed from the PSCs by the PEO-$CH_3NH_3PbI_3$ thin film demonstrates that the trap-filling and ion/vacancy migration are dramatically suppressed [12,13,40]. To further confirm it, the steady state V_{OC} and J_{SC} at the maximum power point (MPP), deriving from PSCs under the forward scan direction and at the scan rate of 0.02 V/s (insert of Fig. 5b), along with the illumination time are measured and the results are shown in Fig. 5b. The PSCs by the PEO-$CH_3NH_3PbI_3$ thin film shows an instant response in the steady-state V_{OC}, J_{SC} and PCE at the MPP; whereas, ~20 s response-time is required to reach the steady-state V_{OC}, J_{SC} and PCE at the MPP for the PSCs by pristine $CH_3NH_3PbI_3$ thin film. In pristine $CH_3NH_3PbI_3$ thin film, a large time scale for ion/vacancy migration before reaching the equilibrium of quasi-steady state conditions, transient effect is responsible for photocurrent hysteresis for the PSCs by pristine $CH_3NH_3PbI_3$ thin film [12,43]. In the PEO-$CH_3NH_3PbI_3$ thin film, the elimination of ion/vacancy migration and ionic involved trapping and de-trapping processes [12,40], consequently renders a significantly minimized photocurrent hysteresis in the PSCs by the PEO-$CH_3NH_3PbI_3$ thin film.

To understand the improved stability of the PSCs by the PEO-$CH_3NH_3PbI_3$ thin film, the UV–vis absorption spectra of un-encapsulated pristine $CH_3NH_3PbI_3$ thin film and the PEO-$CH_3NH_3PbI_3$ thin film, which are tested in an ambient condition with 50% relative humidity at room temperature, are studied. Fig. 5c and d displays the absorption spectra of un-encapsulated pristine $CH_3NH_3PbI_3$ thin film and the PEO-$CH_3NH_3PbI_3$ thin film after certain days exposing in ambient condition with 50% relative humidity at room temperature (time evolution of the absorption spectra is listed in **SI 9**). The absorption edge of pristine $CH_3NH_3PbI_3$ thin film displayed a blue-shift after 6 days, and the intensities of the absorbance in the visible region are gradually reduced,

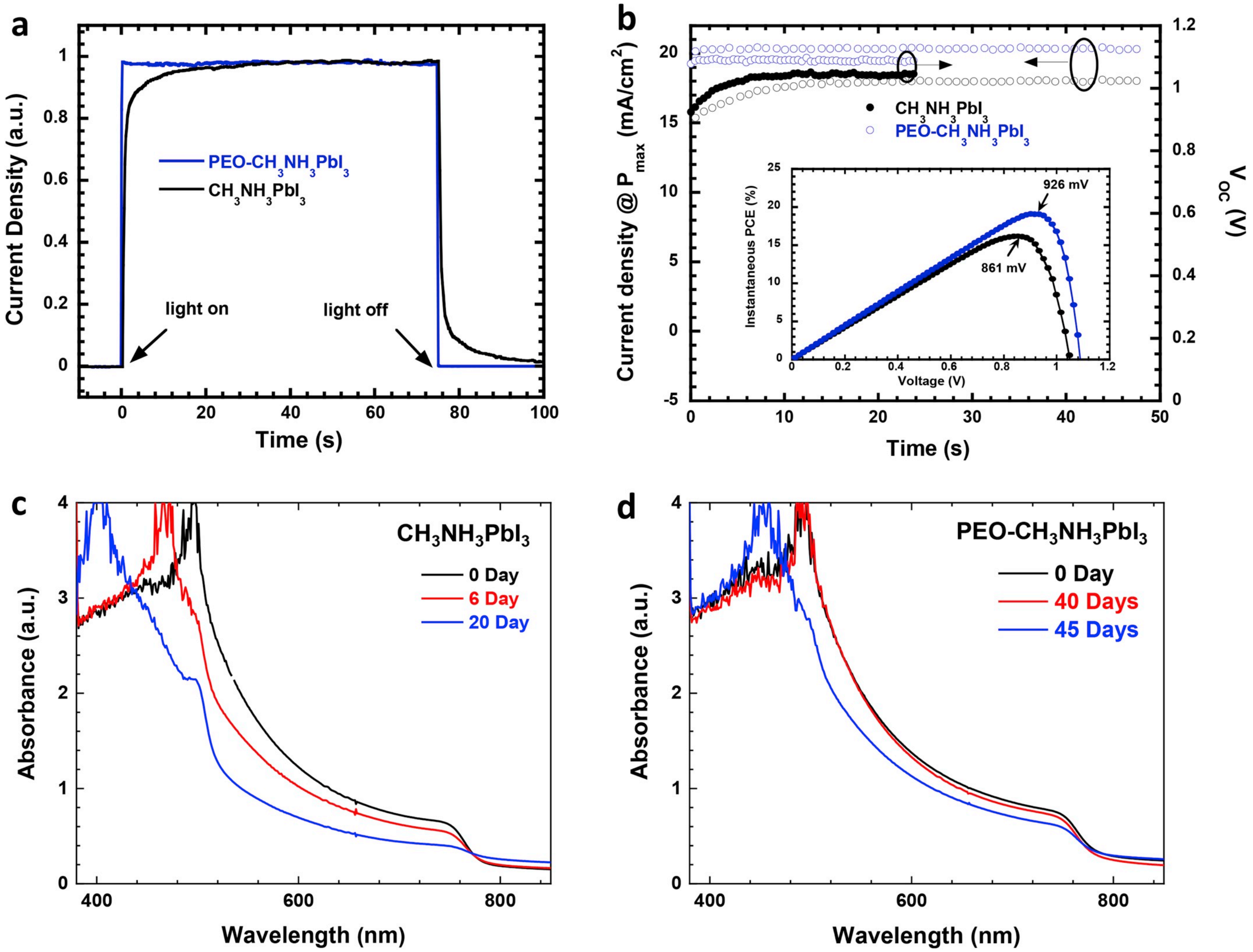

Fig. 5. (a) The photocurrent rising process of PSCs under turn-on/turn-off the incident light, (b) the steady-state V_{OC} and J_{SC} at maximum power point (derived from the J-V curve under forward scan direction and at the scan rate of 0.02 v/s, insert of figure), and normalized absorbance of un-encapsulated thin films of (c) $CH_3NH_3PbI_3$ and (d) PEO-$CH_3NH_3PbI_3$ with different aging times, measured at room temperature in an ambient condition with 50% relative humidity.

implying pristine $CH_3NH_3PbI_3$ thin film is being degraded. After 20 days, the absorption edge is reduced to ~500 nm, which indicates that probably only PbI_2 is left and the $CH_3NH_3^+$ is lost in pristine $CH_3NH_3PbI_3$ thin film. However, the absorption spectrum of the PEO-$CH_3NH_3PbI_3$ thin film being stored for 40 days is almost identical to that of a fresh thin film, indicating that there is nearly no decay in the un-encapsulated PEO-$CH_3NH_3PbI_3$ thin film. After 45 days, the absorption edge started to shift but there still remains an absorption edge at 780 nm. These results collectively demonstrate that the PEO-$CH_3NH_3PbI_3$ thin films are reasonably stable in ambient air with 50% relative humidity at room temperature.

It was reported that $CH_3NH_3PbI_3$ thin films were notoriously sensitive to moisture owning to their ionic characteristics [57]. Various approaches have been attempted to boost the stability of PSCs [57–59], however, less has been done to address the intrinsic disordered lattice patterning, point defects at the atomic-scale, grain boundaries and pin-holes in micro- and/or macro-scale. The enhancement in moisture resistance is attributed to the formation of hydrogen bonding interactions of '$O\cdots H–NH_2CH_3^+$' and '-OH…I-', which passivated the unprotected $CH_3NH_3^+$ cation and I^- anion at the crystal boundaries and shield them from exotic moisture attack. Additionally, the topographical feature of larger contact angle with moisture (**SI 9**), and less pin-holes or grain boundaries for moisture diffusion within the PEO-$CH_3NH_3PbI_3$ thin film offer stronger resistance to moisture as well. Consequently, boosted stability is realized from the PEO-$CH_3NH_3PbI_3$ thin film.

In addition, it is found that the PCE of the PSCs by pristine $CH_3NH_3PbI_3$ thin films vary significantly, ranging from 13.51% to 17.46%. In comparison, the PSCs by the PEO-$CH_3NH_3PbI_3$ thin films exhibit a smaller standard deviation, with a PCE of 18.96 ± 0.19% (SI 13). According to the *t*-distribution, the significantly narrowed confidence interval of 1.01% for PCEs and a confidence level of 95% indicate that the PSCs by the PEO-$CH_3NH_3PbI_3$ thin film possess high reproducibility.

4. Conclusion

In summary, high performance solution-processed perovskites solar cells were demonstrated through development of hybrid perovskite materials co-crystallized with poly (ethylene oxide) (PEO). PEO was used to sequester the mobile counter ions (I^- and $CH_3NH_3^+$) within the crystal lattice, which suppressed the disordered shallow bands and the ion/vacancy migration. It was also found that PEO in perovskite can minimize the point defects, resulting in large crystal growth in a more thermodynamically preferred way. Moreover, the hydrogen interactions between PEO and perovskite lattice reduced the oxygen and moisture percolation pathways, resulting in higher shelf- and thermal-stability for perovskite solar cells. As a result, un-encapsulated solution-processed perovskite solar cells exhibit stabilized power conversion efficiency with hysteresis-free characteristics and significantly improved ambient shelf- and thermal-stability at relative high humidity, in comparison to the reference devices that exhibit unstable power conversion efficiency with dramatically higher hysteresis factor and poorer device lifetime. Our studies demonstrated that development of hybrid perovskite materials co-crystalized with polymers represented a facial way towards high performance perovskites solar cells.

Declaration of competing interest

The authors declare no competing financial interest.

Acknowledgements

The authors acknowledge Air Force Office of Scientific Research (through the Organic Materials Chemistry Program, Grant Number: FA9550-15-1-0292, Program Manager, Dr. Kenneth Caster) and National Science Foundation (EECS 1351785 and EECS 1903303) for financial supports. The authors thank Dr. Zhang Jiang and Dr. Joseph W. Strzalka at Argonne National Laboratory for assistance with the GIWAXS measurements through the U.S. Department of Energy, Office of Science, Office of Basic Energy Sciences, under Contract DE-AC02-06CH11357.

Appendix A. Supplementary data

Supplementary data to this article can be found online at https://doi.org/10.1016/j.nanoen.2019.104229.

References

[1] M. Grätzel, Acc. Chem. Res. 50 (2017) 487–491, https://doi.org/10.1021/acs.accounts.6b00492.
[2] J. Seo, J.H. Noh, S.I. Seok, Acc. Chem. Res. 49 (2016) 562–572, https://doi.org/10.1021/acs.accounts.5b00444.
[3] L.M. Pazos-Outón, M. Szumilo, R. Lamboll, J.M. Richter, M. Crespo-Quesada, M. Abdi-Jalebi, H.J. Beeson, M. Vrućinić, M. Alsari, H.J. Snaith, Science 351 (2016), https://doi.org/10.1126/science.aaf1168.
[4] L.M. Herz, Annu. Rev. Phys. Chem. 67 (2016) 65–89, https://doi.org/10.1146/annurev-physchem-040215-112222.
[5] A. Walsh, D.O. Scanlon, S. Chen, X. Gong, S.H. Wei, Angew. Chem. 54 (2015) 1791–1794, https://doi.org/10.1002/anie.201409740.
[6] J.-P. Correa-Baena, A. Abate, M. Saliba, W. Tress, T.J. Jacobsson, M. Grätzel, A. Hagfeldt, Science 358 (2017) 739–744, https://doi.org/10.1126/science.aam6323.
[7] F.A. Kroger, The Chemistry of Imperfect Crystals, North-Holland Pub. Co., 1974.
[8] A. Buin, P. Pietsch, J. Xu, O. Voznyy, A.H. Ip, R. Comin, E.H. Sargent, Nano Lett. 14 (2014) 6281–6286, https://doi.org/10.1021/nl502612m.
[9] M.L. Agiorgousis, Y.-Y. Sun, H. Zeng, S. Zhang, J. Am. Chem. Soc. 136 (2014) 14570–14575, https://doi.org/10.1021/ja5079305.
[10] F. Brivio, A.B. Walker, A. Walsh, Apl. Mater. 1 (2013), 042111, https://doi.org/10.1063/1.4824147.
[11] A. Dualeh, T. Moehl, N. Tétreault, J. Teuscher, P. Gao, M.K. Nazeeruddin, M. Grätzel, ACS Nano 8 (2013) 362–373, https://doi.org/10.1021/nn404323g.
[12] C. Eames, J.M. Frost, P.R. Barnes, B.C. O'regan, A. Walsh, M.S. Islam, Nat. Commun. 6 (2015) 7497, https://doi.org/10.1038/ncomms8497.
[13] H.J. Snaith, A. Abate, J.M. Ball, G.E. Eperon, T. Leijtens, N.K. Noel, S.D. Stranks, J. T.-W. Wang, K. Wojciechowski, W. Zhang, J. Phys. Chem. Lett. 5 (2014) 1511–1515, https://doi.org/10.1021/jz500113x.
[14] Y. Rong, L. Liu, A. Mei, X. Li, H. Han, Adv. Energy Mater. 5 (2015) 1501066, https://doi.org/10.1002/aenm.201501066.
[15] E.T. Hoke, D.J. Slotcavage, E.R. Dohner, A.R. Bowring, H.I. Karunadasa, M. D. McGehee, Chem. Sci. 6 (2015) 613–617, https://doi.org/10.1039/C4SC03141E.
[16] S. Masi, A. Rizzo, R. Munir, A. Listorti, A. Giuri, C. Esposito Corcione, N.D. Treat, G. Gigli, A. Amassian, N. Stingelin, Adv. Energy Mater. 7 (2017) 1602600, https://doi.org/10.1002/aenm.201602600.
[17] C.-C. Zhang, M. Li, Z.-K. Wang, Y.-R. Jiang, H.-R. Liu, Y.-G. Yang, X.-Y. Gao, H. Ma, J. Mater. Chem. A 5 (2017) 2572–2579, https://doi.org/10.1039/C6TA08970D.
[18] M.K. Sardashti, M. Zendehdel, N.Y. Nia, D. Karimian, M. Sheikhi, Chem. Sus. Chem. 10 (2017) 3773–3779, https://doi.org/10.1002/cssc.201701027.
[19] Y. Zhao, J. Wei, H. Li, Y. Yan, W. Zhou, D. Yu, Q. Zhao, Nat. Commun. 7 (2016) 10228, https://doi.org/10.1038/ncomms10228.
[20] Y. Guo, K. Shoyama, W. Sato, E. Nakamura, Adv. Energy Mater. 6 (2016) 1502317, https://doi.org/10.1002/aenm.201502317.
[21] D. Bi, C. Yi, J. Luo, J.-D. Décoppet, F. Zhang, S.M. Zakeeruddin, X. Li, A. Hagfeldt, M. Grätzel, Nat. Energy 1 (2016) 16142, https://doi.org/10.1038/nenergy.2016.142.
[22] J. Jiang, Q. Wang, Z. Jin, X. Zhang, J. Lei, H. Bin, Z.G. Zhang, Y. Li, S. Liu, Adv. Energy Mater. 8 (2018) 1701757, https://doi.org/10.1002/aenm.201701757.
[23] K. Wang, L. Zheng, T. Zhu, X. Yao, C. Yi, X. Zhang, Y. Cao, L. Liu, W. Hu, X. Gong, Nano Energy 61 (2019) 352–360, https://doi.org/10.1016/j.nanoen.2019.04.073.
[24] Z. Jiang, X. Li, J. Strzalka, M. Sprung, T. Sun, A.R. Sandy, S. Narayanan, D.R. Lee, J. Wang, J. Synchrotron Radiat. 19 (2012) 627–636, https://doi.org/10.1107/S0909049512022017.
[25] W. Xu, L. Zheng, X. Zhang, Y. Cao, T. Meng, D. Wu, L. Liu, W. Hu, X. Gong, Adv. Eng. Mater. 8 (2018) 1703178, https://doi.org/10.1002/aenm.201703178.
[26] B.R. Vincent, K.N. Robertson, T.S. Cameron, O. Knop, Can. J. Chem. 65 (1987) 1042–1046, https://doi.org/10.1139/v87-176.
[27] G.R. Desiraju, T. Steiner, The Weak Hydrogen Bond: in Structural Chemistry and Biology, International Union of Crystal, 2001.
[28] M.M. Coleman, D.J. Skrovanek, J. Hu, P.C. Painter, Macromolecules 21 (1988) 59–65, https://doi.org/10.1007/BF01507527, 10.1021/ma00179a014.
[29] X. Li, M.I. Dar, C. Yi, J. Luo, M. Tschumi, S.M. Zakeeruddin, M.K. Nazeeruddin, H. Han, M. Grätzel, Nat. Chem. 7 (2015) 703–711, https://doi.org/10.1038/nchem.2324.
[30] H. Tsai, R. Asadpour, J.-C. Blancon, C.C. Stoumpos, O. Durand, J.W. Strzalka, B. Chen, R. Verduzco, P.M. Ajayan, S. Tretiak, Science 360 (2018) 67–70, https://doi.org/10.1126/science.aap8671.
[31] M.H. Li, H.H. Yeh, Y.H. Chiang, U.S. Jeng, C.J. Su, H.W. Shiu, Y.J. Hsu, N. Kosugi, T. Ohigashi, Y.A. Chen, Adv. Mater. 30 (2018) 1801401, https://doi.org/10.1002/adma.201801401.
[32] D.T. Toolan, A. Isakova, R. Hodgkinson, N. Reeves-McLaren, O.S. Hammond, K. J. Edler, W.H. Briscoe, T. Arnold, T. Gough, P.D. Topham, Macromolecules 49 (2016) 4579–4586, https://doi.org/10.1021/acs.macromol.6b00312.
[33] K. Busse, C. Fuchs, N. Hasan, M. Pulst, J.R. Kressler, Langmuir 34 (2018) 12759–12763, https://doi.org/10.1021/acs.langmuir.8b02451.
[34] J. Novoa, Intermolecular Interactions in Crystals: Fundamentals of Crystal Engineering, Royal Society of Chemistry, 2017.
[35] Y. Saruyama, J. Chem. Phys. 78 (1983) 2077–2080, https://doi.org/10.1063/1.444916.
[36] D.W. Oxtoby, Acc. Chem. Res. 31 (1998) 91–97, https://doi.org/10.1021/ar9702278.
[37] S.-Y. Chung, Y.-M. Kim, J.-G. Kim, Y.-J. Kim, Nat. Phys. 5 (2009) 68–73, https://doi.org/10.1038/nphys1148.
[38] J.-W. Lee, H.-S. Kim, N.-G. Park, Acc. Chem. Res. 49 (2016) 311–319, https://doi.org/10.1021/acs.accounts.5b00440.
[39] R.S. Sanchez, V. Gonzalez-Pedro, J.-W. Lee, N.-G. Park, Y.S. Kang, I. Mora-Sero, J. Bisquert, J. Phys. Chem. Lett. 5 (2014) 2357–2363, https://doi.org/10.1021/jz5011187.
[40] K. Miyano, M. Yanagida, N. Tripathi, Y. Shirai, J. Phys. Chem. Lett. 7 (2016) 2240–2245, https://doi.org/10.1021/acs.jpclett.6b00579.
[41] H.-S. Kim, I.-H. Jang, N. Ahn, M. Choi, A. Guerrero, J. Bisquert, N.-G. Park, J. Phys. Chem. Lett. 6 (2015) 4633–4639, https://doi.org/10.1021/acs.jpclett.5b02273.
[42] S. van Reenen, M. Kemerink, H.J. Snaith, J. Phys. Chem. Lett. 6 (2015) 3808–3814, https://doi.org/10.1021/acs.jpclett.5b01645.
[43] S.R. Cowan, R. Street, S. Cho, A. Heeger, Phys. Rev. B 83 (2011) 035205, https://doi.org/10.1103/PhysRevB.83.035205.
[44] J. Seifter, Y. Sun, H. Choi, B.H. Lee, T.L. Nguyen, H.Y. Woo, A.J. Heeger, Adv. Mater. 27 (2015) 4989–4996, https://doi.org/10.1002/adma.201500416.
[45] J. Bisquert, Phys. Chem. Chem. Phys. 10 (2008) 49–72, https://doi.org/10.1039/B709316K.
[46] Z. Pomerantz, A. Zaban, S. Ghosh, J.-P. Lellouche, G. Garcia-Belmonte, J. Bisquert, J. Electroanal. Chem. 614 (2008) 49–60, https://doi.org/10.1016/j.jelechem.2007.11.005.
[47] H. Bässler, Phys. Status Solidi (b) 175 (1993) 15–56, https://doi.org/10.1002/pssb.2221750102.
[48] J. Bisquert, F. Fabregat-Santiago, I. Mora-Sero, G. Garcia-Belmonte, E.M. Barea, E. Palomares, Inorg. Chim. Acta 361 (2008) 684–698, https://doi.org/10.1016/j.ica.2007.05.032.
[49] W.L. Leong, S.R. Cowan, A.J. Heeger, Adv. Energy Mater. 1 (2011) 517–522, https://doi.org/10.1002/aenm.201100196.
[50] C.G. Shuttle, B. O'Regan, A.M. Ballantyne, J. Nelson, D.D. Bradley, J.R. Durrant, Phys. Rev. B 78 (2008) 113201, https://doi.org/10.1103/PhysRevB.78.113201.
[51] C. Groves, N. Greenham, Phys. Rev. B 78 (2008) 155205, https://doi.org/10.1103/PhysRevB.78.155205.
[52] R. Street, M. Schoendorf, A. Roy, J. Lee, Phys. Rev. B 81 (2010) 205307, https://doi.org/10.1103/PhysRevB.81.205307.
[53] C. Liu, K. Wang, C. Yi, X. Shi, A.W. Smith, X. Gong, A.J. Heeger, Adv. Funct. Mater. 26 (2016) 101–110, https://doi.org/10.1002/adfm.201504041.
[54] G. Garcia-Belmonte, P.P. Boix, J. Bisquert, M. Sessolo, H.J. Bolink, Sol. Energy Mater. Sol. Cells 94 (2010) 366–375, https://doi.org/10.1016/j.solmat.2009.10.015.
[55] J. Bisquert, A. Zaban, M. Greenshtein, I. Mora-Seró, J. Am. Chem. Soc. 126 (2004) 13550–13559, https://doi.org/10.1021/ja047311k.
[56] J. Bisquert, D. Cahen, G. Hodes, S. Rühle, A. Zaban, J. Phys. Chem. B 108 (2004) 8106–8118, https://doi.org/10.1021/jp0359283.

[57] G. Niu, X. Guo, L. Wang, J. Mater. Chem. A 3 (2015) 8970–8980, https://doi.org/10.1039/C4TA04994B.

[58] J. You, L. Meng, T.-B. Song, T.-F. Guo, Y.M. Yang, W.-H. Chang, Z. Hong, H. Chen, H. Zhou, Q. Chen, Nat. Nanotechnol. 11 (2016) 75–81, https://doi.org/10.1038/nnano.2015.230.

[59] I.C. Smith, E.T. Hoke, D. Solis-Ibarra, M.D. McGehee, H.I. Karunadasa, Angew. Chem. 53 (2014) 11232–11235, https://doi.org/10.1002/anie.201406466.